

## Census of young stellar population in the Galactic H II region Sh2-242

ALIK PANJA,<sup>1</sup> SOUMEN MONDAL,<sup>1</sup> SOMNATH DUTTA,<sup>2</sup> SANTOSH JOSHI,<sup>3</sup> SNEH LATA,<sup>3</sup> AND RAMKRISHNA DAS<sup>1</sup>

<sup>1</sup>*S. N. Bose National Centre for Basic Sciences, Kolkata 700106, India*

<sup>2</sup>*Institute of Astronomy and Astrophysics, Academia Sinica, Taipei 10617, Taiwan*

<sup>3</sup>*Aryabhata Research Institute of Observational Sciences, Nainital 263002, India*

(Received ...; Revised ...; Accepted ...)

Submitted to AJ

### ABSTRACT

We present here identification and characterization of the young stellar population associated with an active star-forming site Sh2-242. We used our own new optical imaging and spectroscopic observational data, as well as several archival catalogs, e.g., Pan-STARRS 1, *Gaia* DR2, IPHAS, WIRCam, 2MASS, and *Spitzer*. Slit spectroscopic results confirm the classification of the main ionizing source BD+26 980 as an early-type star of spectral type B0.5 V. The spectrophotometric distance of the star is estimated as  $2.08 \pm 0.24$  kpc, which confirms the source as a member of the cluster. An extinction map covering a large area (diameter  $\sim 50'$ ) is generated with *H* and *K* photometry toward the region. From the map, three distinct locations of peak extinction complexes ( $A_V \simeq 7\text{--}17$  mag) are identified for the very first time. Using the infrared color excess, a total of 33 Class I and 137 Class II young objects are classified within the region. The IPHAS photometry reveals classification of 36 H $\alpha$  emitting sources, which might be class II objects. Among 36 H $\alpha$  emitting sources, 5 are already identified using infrared excess emission. In total, 201 young objects are classified toward S242 from this study. The membership status of the young sources is further windowed with the inclusion of parallax from the *Gaia* DR2 catalog. Using the optical and infrared color-magnitude diagrams, the young stellar objects are characterized with an average age of  $\sim 1$  Myr and the masses in the range  $0.1\text{--}3.0 M_\odot$ . The census of the stellar content within the region is discussed using combined photometric and spectroscopic data.

*Keywords:* stars: formation – stars: pre-main-sequence – H II regions – ISM: individual objects: Sh2-242.

### 1. INTRODUCTION

Stellar clusters are recognized as promising astrophysical sites as their formation and early evolution take place primarily in the Galactic spiral arms (Lada & Lada 2003). Systematic studies of young clusters probe several dominant astrophysical problems, such as the formation of stars and planetary systems to the evolution of open clusters (Adams et al. 2006; Adams 2010; Santos-Silva et al. 2012). Most of the stars originate in populous groups within giant regions of molecular clouds (Carpenter 2000; Palla & Stahler 2002; Porras et al. 2003). Massive stars ( $>8 M_\odot$ ) play an immense role to create

a birthplace for next generation stars by emitting huge amounts of energy in the ultraviolet range (Elmegreen & Lada 1977). The Lyman continuum radiation gradually ionizes the surrounding interstellar medium (ISM) and create H II regions. The newly formed H II regions are the zero-age objects compared with the age of the Milky Way and are thus efficient tracers of star formation at the present epoch (Anderson et al. 2014). Zones of H II regions are presumed to be the productive sites of second generation star formation (Elmegreen 1998). The early phases of stellar evolution occur within the dense regions of molecular clouds, where young stellar populations are invariably associated with significant amounts of interstellar dust and gas (Lada & Adams 1992). Young stars associated in a cluster are thought to have formed almost simultaneously from the same

progenitor molecular cloud and share similar heritage of age, distance, and chemical composition (Fukuda & Hanawa 2000). The infrared and radio wavelength surveys provide the global pictures of young star-forming regions and their formation scenarios. However, the parameters of a young cluster can be estimated from the optical/infrared photometric study of the stellar sources and the spectroscopic data of massive exciting stars associated with the cluster. Despite recent advancements in observational and theoretical prospects, the complete star formation census is still poorly understood and requires further exploration.

In this context, we present a multiwavelength survey of the Galactic H II region Sh2-242 (S242;  $\alpha_{(2000)} = 05^{\text{h}}51^{\text{m}}54^{\text{s}}$ ,  $\delta_{(2000)} = +27^{\circ}01'54''$ ), located in the Taurus constellation. Mayer & Macák (1973) first classified the main ionizing source of the region, BD+26 980 as spectral type B0 V. Using *UBV* photoelectric photometry, they overestimated the distance of the star as 3.39 kpc. Using the spectroscopic observations and  $\text{H}\gamma$  equivalent widths, Crampton & Fisher (1974) also estimated the spectral type of BD+26 980 as B0 V. Using the absolute magnitude from spectroscopic classification and assuming the ratio of total-to-selective absorption as 3.0, the authors calculated the distance of the star as 2.1 kpc. Using *UBVRI* photometric observations, Lahulla (1987) estimated the distance to the exciting star to be 2.5 kpc and the extinction as 2.4 mag [ $E(B - V) = 0.76$  mag]. To estimate the distance, they used an absolute magnitude based on a B0 V spectral type and assuming  $A_V/E(B - V) = 3.1$  or using the MK spectral types. Hunter & Massey (1990) classified the spectral type of BD+26 980 to be B0 V using optical spectroscopy. They estimated the distance to be 2.7 kpc using simulated *B* and *V* photometry formed from the optical spectra of the star.

Together, these previous studies indicate that the young cluster S242 is an active site of star formation and also harbors a massive star of spectral type B0 V. In this paper, we present a multiwavelength study on the identification and characterization of the young stellar population toward this region. In Section 2, we describe the observational and archival data sets used, including their reduction processes. Section 3 comprises the results of spectroscopically observed bright sources and identification and classification of young stellar objects (YSOs) using archival data sets. Characterization of YSOs, such as spectral nature, age, and mass spectrum, and the cluster properties are discussed in Section 4. The final results are summarized and concluded in Section 5.

## 2. DATA SETS AND REDUCTION

### 2.1. New Observations

#### 2.1.1. Optical Photometry

Optical photometric data for *B* (360 nm), *V* (550 nm), and *I* (900 nm) bands were acquired with the 1.3 m Devasthal Fast Optical Telescope (DFOT; Sagar et al. 2012), Nainital, India, with different exposure times to cover bright to faint sources. The photometric observations were carried out using a 13.5 micron pixel, 2K×2K Andor CCD camera, which covers a square area of about  $18' \times 18'$  on the sky with a plate scale of  $0''.53 \text{ pixel}^{-1}$ . The CCD has a readout noise and gain of  $7 e^-$  and  $2.2 e^- \text{ ADU}^{-1}$  respectively. During the observations, the average seeing was  $\sim 2''$ . The photometric standard field SA 95 (Landolt 1992) was observed on the same night with different airmass, to apply atmospheric and instrumental corrections to the target frames. The log of optical photometric observations is given in Table 1. The color composite image (blue: *B*, green: *V*, and red: *I*) generated from optical observations toward the S242 region is shown in the Fig. 1(a). The sources marked with yellow circles represent the stars observed with slit spectroscopy (see Section 2.1.2) and their corresponding ID numbers (Table 1) are given. The optical/infrared three color image generated from DSS2 *R* 0.70  $\mu\text{m}$  (blue), 2MASS *K* 2.2  $\mu\text{m}$  (green), and *WISE W2* 4.6  $\mu\text{m}$  (red) for the region is shown in the Fig. 1(b). The main illuminating source BD+26 980 is depicted in both the panels.

Optical photometric data were reduced using sophisticated tasks from the IRAF<sup>1</sup> software. The raw CCD images were cleaned by subtracting the median combination of bias and flat frames, following cosmic ray removal. Point sources were extracted using the DAOFIND task from the DAOPHOT package with necessary sky background and detection threshold limits. A point-spread function (PSF) fitting algorithm was performed on all the sources using the ALLSTAR routine (Stetson 1987). Atmospheric extinction and color coefficients were calculated from observations of the standard field for corresponding filters by fitting a linear least-squares fit regression method (Stetson 1992). A set of transformation equations (Equations 1, 2, and 3) were used to convert the instrumental magnitudes to the standard systems as follows.

$$(B - V) = m_{bv}(b - v) + c_{bv} \quad (1)$$

<sup>1</sup> Image Reduction and Analysis Facility (IRAF) (<http://iraf.noao.edu/>)

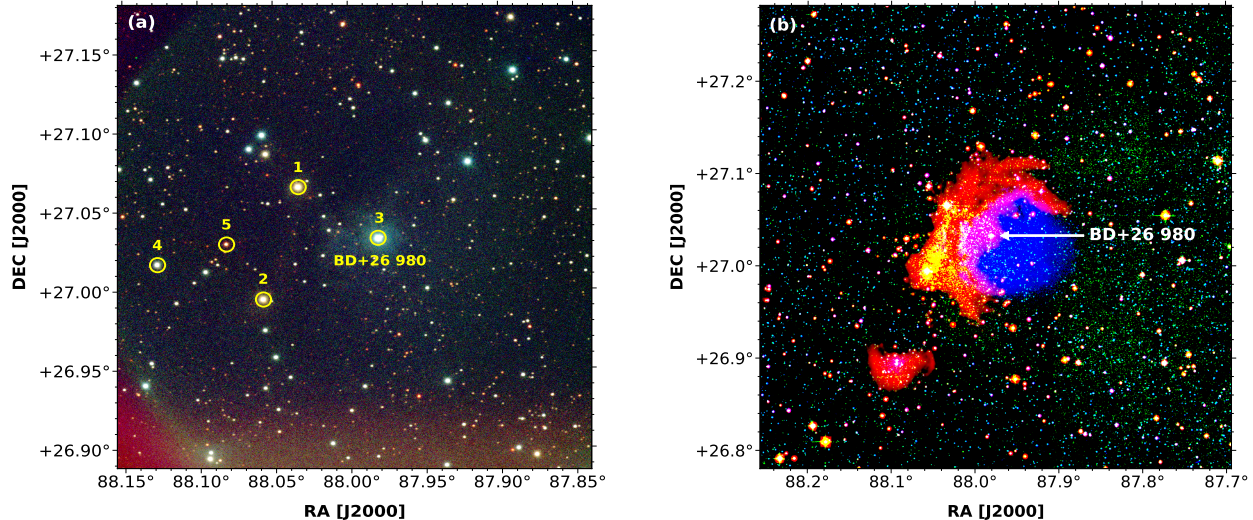


**Figure 1.** (a) Optical color composite image of the S242 region, created with  $B$  360 nm (blue),  $V$  550 nm (green), and  $I$  900 nm (red) bands for a sky area of  $18 \times 18$  arcmin<sup>2</sup>, acquired with the 1.3 m DFOT. Spectroscopically observed sources from the 2 m HCT are numbered and marked with yellow circles and the main ionizing source BD+26 980 is depicted. (b) Color composite image of the S242 cluster with optical and infrared counterparts taken from DSS2  $R$  0.70  $\mu$ m (blue), 2MASS  $K$  2.2  $\mu$ m (green), and *WISE*  $W2$  4.6  $\mu$ m (red) bands.

**Table 1.** Log of Optical Photometric and Spectroscopic Observations.

ID	R.A. (J2000) (h:m:s)	Decl. (J2000) (d:m:s)	Date of Observations	Filter/ Grism	Exp. time (s) $\times$ No. of frames	Airmass/ SNR	$V$ (mag)	$B - V$ (mag)
Photometry								
Sh2-242	05:52:20	+27:02:30	2016 Dec 19	$B$	500 $\times$ 3, 60 $\times$ 3	1.018		
Sh2-242	05:52:20	+27:02:30	2016 Dec 19	$V$	500 $\times$ 3, 60 $\times$ 3	1.679		
Sh2-242	05:52:20	+27:02:30	2016 Dec 19	$I$	300 $\times$ 3, 10 $\times$ 3	1.130		
Slit Spectroscopy								
1	05:52:08.13	+27:03:55.64	2016 Nov 03	7, 8	900 $\times$ 1, 900 $\times$ 1	18, 27	10.864	1.608
2	05:52:13.83	+26:59:40.83	2016 Nov 03	7, 8	1200 $\times$ 1, 1200 $\times$ 1	20, 28	11.313	1.451
3	05:51:55.41	+27:01:58.03	2016 Nov 03	7, 8	1200 $\times$ 1, 900 $\times$ 1	29, 41	10.128	0.483
4	05:52:30.68	+27:01:01.15	2017 Jan 23	7, 8	1800 $\times$ 1, 1800 $\times$ 1	24, 26	11.978	0.914
5	05:52:19.65	+27:01:46.83	2017 Jan 23	7, 8	1800 $\times$ 1, 1800 $\times$ 1	14, 17	14.246	1.879
Slitless Spectroscopy								
Sh2-242_1	05:52:24.03	+26:58:29.57	2017 Dec 15	Gr5/H $\alpha$ -Br	1800 $\times$ 1	1.273		
Sh2-242_2	05:51:44.16	+26:58:38.72	2017 Dec 15	Gr5/H $\alpha$ -Br	1800 $\times$ 1	1.361		
Sh2-242_3	05:51:44.34	+27:07:36.12	2017 Dec 15	Gr5/H $\alpha$ -Br	1800 $\times$ 1	1.657		
Sh2-242_4	05:52:24.45	+27:07:31.31	2017 Dec 15	Gr5/H $\alpha$ -Br	1800 $\times$ 1	1.882		

$$(V - I) = m_{vi}(v - i) + c_{vi} \quad (2)$$

and

$$V = v + m_v(V - I) + c_v \quad (3)$$

where  $B$ ,  $V$ , and  $I$  are the magnitudes in standard systems and  $b$ ,  $v$ , and  $i$  are instrumental magnitudes corrected for the atmospheric extinction due to airmass. The details of color coefficients ( $m_{bv}$ ,  $m_{vi}$ ,  $m_v$ ), constant terms ( $c_{bv}$ ,  $c_{vi}$ ,  $c_v$ ), and extinction coefficients ( $K_b$ ,  $K_v$ ,  $K_i$ ) are tabulated in Table 2.

A total of 12 standard stars was used to calculate the color coefficients and zero-point constants in the standard field. Fig. 2 shows the variation of residuals between transformed and standard colors and magnitudes as a function of  $V$  magnitude.

The world coordinate system on the physical frames was obtained by selecting 24 unsaturated, isolated, and moderately bright stars from the 2MASS catalog for the same field. We used the IRAF tasks CCMAP, and CCSETWCS and the WCSTOOLS package to obtain the astrometric solutions.

**Table 2.** Color coefficients, constant terms, and extinction coefficients used for optical photometric calibrations.

Parameters	Constants
Color coefficients	
$m_{bv}$	$1.326 \pm 0.023$
$m_{vi}$	$0.897 \pm 0.014$
$m_v$	$-0.125 \pm 0.011$
Zero-point constants	
$c_{bv}$	$-1.019 \pm 0.027$
$c_{vi}$	$0.384 \pm 0.016$
$c_v$	$-2.024 \pm 0.013$
Extinction coefficients	
$K_b$	$0.262 \pm 0.010$
$K_v$	$0.229 \pm 0.005$
$K_i$	$0.103 \pm 0.005$

### 2.1.2. Optical Slit Spectroscopy

Optical slit spectroscopic observations for five bright sources within the region were carried out using the Himalaya Faint Object Spectrograph and Camera (HFOSC) on the 2 m Himalayan Chandra Telescope (HCT). Spectra were taken with Grism 7 (380 - 684 nm) and Grism 8 (580 - 830 nm) with resolutions of 1330 and 2190, respectively. The spectroscopic standard star Feige 34 (Oke 1990) was observed on the same night for flux calibration. The FeAr and FeNe arc lamp observations were conducted immediately after the target observations for wavelength calibration. The log of optical spectroscopic observations is shown in Table 1.

After being rectified by bias subtraction and cosmic ray correction, the monodimensional spectra were extracted using the APALL task in the IRAF software. The spectra were then wavelength calibrated from corresponding lamp observations. The data were corrected for atmospheric extinction and instrument sensitivity availing the standard star observations.

### 2.1.3. Optical Slitless Spectroscopy

Slitless spectroscopic data were obtained from the HCT to detect  $H\alpha$  emission line stars toward the region. The data were acquired using a broadband  $H\alpha$  filter (630 - 674 nm) in combination with Grism 5 (520 - 1030 nm) in slitless mode (Table 1). The  $2K \times 2K$  CCD has a field of view (FOV) of  $10 \times 10$  arcmin<sup>2</sup> with an image scale of  $0''.296$  pixel<sup>-1</sup>. The resolution of Grism 5 is 870. The data were taken for four overlapping frames covering a total sky area ( $18' \times 18'$ ) similar to that of the optical photometric observations (Section 2.1.1). The  $H\alpha$  emitting sources show certain enhancements in their spectra over the continuum. We have visually identified

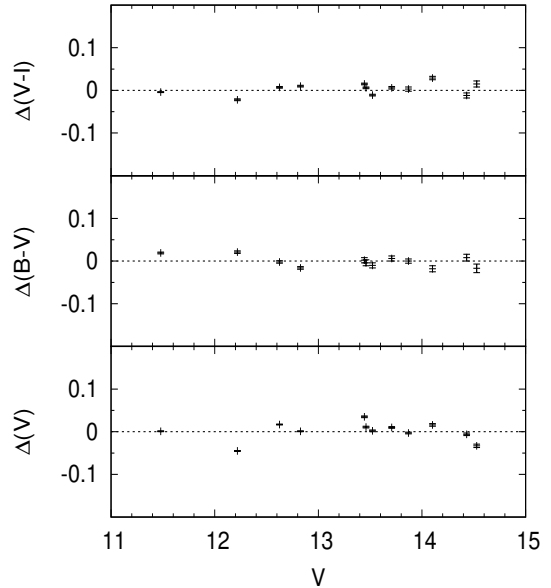


**Figure 2.** Plot of residuals between transformed colors and magnitudes with standard values as a function of standard  $V$  magnitudes.

three sources having prominent  $H\alpha$  emissions from these observations.

### 2.2. Optical/NIR Photometry from Pan-STARRS 1

As a complementary data set to the observed optical photometry (Section 2.1.1), we used optical/NIR imaging from the Panoramic Survey Telescope and Rapid Response System 1 (Pan-STARRS 1, or PS1; Chambers et al. 2019). The PS1 camera consists of a mosaic of 60 edge-abutted  $4846 \times 4868$  pixel detectors, with  $10 \mu\text{m}$  pixels subtending  $0''.258$ . The PS1 provides homogeneous and deeper coverage photometry in five broad passbands  $g_{P1}$ ,  $r_{P1}$ ,  $i_{P1}$ ,  $z_{P1}$ , and  $y_{P1}$ , ranging from 400 nm to 1000 nm (Stubbs et al. 2010). The effective wavelengths for the five filters are roughly 480, 620, 750, 870, and 960 nm, respectively, similar to those used by the SDSS (York et al. 2000), with most significant difference being the replacement of the Sloan  $u$  band with a NIR band  $y_{P1}$ . The PS1 image processing, astrometry, and photometry are detailed in Magnier et al. (2016a,b) and the relative and absolute calibration survey are reported in Schlafly et al. (2012) and Tonry et al. (2012). The typical single-epoch  $5\sigma$  photometric depths in the corresponding five passbands are 22.0, 21.8, 21.5, 20.9, and 19.7 mag (AB), respectively (Chambers et al. 2019). The empirical components of the adopted extinction vector are taken from Schlafly et al. (2016) and given in Table 3.

### 2.3. Archival Data from Gaia DR2

**Table 3.** Extinction vector,  $R$ , adopted in this work for the Pan-STARRS 1 catalog, are based on Schlafly et al. (2016).

$g_{P1}$	$r_{P1}$	$i_{P1}$	$z_{P1}$	$y_{P1}$
3.384	2.483	1.838	1.414	1.126

The *Gaia* Data Release 2 (*Gaia* DR2; Gaia Collaboration et al. 2018) provides five parameter (position, proper motion, and parallax) astrometric results for over 1.3 billion sources from the observations of the European Space Agency *Gaia* satellite (Gaia Collaboration et al. 2016). The parallaxes of the sources toward the S242 cluster are collected from the *Gaia* DR2 archive<sup>2</sup>. The distance and membership status of the sources are estimated by restricting the data to only positive parallaxes. The positive parallaxes with relative uncertainties typically below 20% are primarily considered as reliable astrometry (Luri et al. 2018).

#### 2.4. Archival Data from IPHAS DR2

The INT/WFC Photometric H $\alpha$  Survey of the Northern Galactic Plane (IPHAS; Drew et al. 2005) is an imaging survey covering an 1800 deg<sup>2</sup> sky in broadband Sloan  $r$  (624 nm) and  $i$  (774.3 nm), and narrowband H $\alpha$  (656.8 nm) filters using the Wide Field Camera (WFC) on the 2.5 m Isaac Newton Telescope (INT) in La Palma. The WFC generates a mosaic of four CCDs at a pixel scale of 0''.33 pixel<sup>-1</sup>. This survey offers an unique facility to detect H $\alpha$  emission line objects by comprehensive CCD photometry of point sources at visible wavelengths. The photometric data for  $r$ ,  $i$ , and H $\alpha$  bands were obtained from the IPHAS DR2 catalog (Barentsen et al. 2014) for the S242 cluster.

#### 2.5. Infrared Archival Data

##### 2.5.1. Near-Infrared Data: WIRCam and 2MASS

The Wide-field InfraRed Camera (WIRCam; Puget et al. 2004) is the NIR mosaic imager mounted at the prime focus of the 3.6 m Canada-France-Hawaii Telescope (CFHT) on Maunakea, Hawaii. The WIRCam consists of four 2048 $\times$ 2048 HAWAII2-RG detectors covering a field of view of 20 arcmin<sup>2</sup> with a pixel scale of 0''.3. The deep NIR images in  $J$  (1.25  $\mu$ m),  $H$  (1.63  $\mu$ m), and  $K$  (2.14  $\mu$ m) bands<sup>3</sup> for the S242 region were collected from the CFHT archive<sup>4</sup> for Proposal ID 06BF14 and 06BF96, respectively. The observations were carried out under principal investigator Lise Deharveng on December 28, 2006 and January 01, 2007 accordingly. The

raw data were optimized using the Interactive Data Language (IDL) based interface the SIMPLE Imaging and Mosaicking Pipeline (SIMPLE; Wang et al. 2010). The astrometric and photometric reductions were performed in a similar way, as are outlined in Dutta et al. (2018). Briefly the dithered images were mosaicked using median combination technique. The astrometric calibrations of the combined images were performed in comparison with the 2MASS reference frames. The point sources in the reduced astrometric frames were identified by using PSF fitting algorithm from the DAOFIND package (Stetson 1992) in the IRAF software. Photometric calibrations of the WIRCam frames were performed in comparison with the 2MASS catalog considering all the sources with magnitude uncertainty < 0.1 mag.

The 2MASS Point Source Catalog (PSC; Skrutskie et al. 2006) photometry in  $J$ ,  $H$ , and  $K$  bands were taken as a complementary data set. In an attempt to avoid the inclusion of saturated sources in WIRCam photometry, we replaced all the sources in WIRCam with 2MASS magnitudes for  $J$  < 13 mag,  $H$  < 12.5 mag, and  $K$  < 12 mag (Dutta et al. 2018). A photometric uncertainty < 0.1 mag for all the bands was considered as quality criteria for reliable photometry, which provides S/N  $\geq$  10.

##### 2.5.2. Mid-Infrared Data: Spitzer

We obtained MIR photometry for point sources toward the S242 region from the *Spitzer* Warm Mission (Hora et al. 2012) survey. Magnitudes from the Infrared Array Camera (IRAC; Fazio et al. 2004) [3.6] and [4.5]  $\mu$ m bands with a pixel scale of 1''.2 pixel<sup>-1</sup> were downloaded from the highly reliable Glimpse360<sup>5</sup> catalog (Program Id: 61070, PI: Whitney, Barbara A). We restricted the sources with photometric uncertainty  $\sigma$  < 0.2 mag for all the IRAC bands to achieve good quality photometric catalog.

#### 2.6. Multiwavelength Catalog

The final catalog was generated by matching different optical to infrared data sets in stages. The *BVI* catalog was built by cross-matching all the sources detected from optical photometry (Section 2.1.1) with a radial tolerance of 2''. As the seeing ( $\sim$  2'') was not sufficiently good, we used a matching radius of 2'' to match the sources detected in optical photometry. We performed several test matches by increasing the radial distance from 1'' to 3'' in steps of 0''.1 to pick up the suitable matching radius for each catalog data. In case of multiple sources matched within a given matching radius, we

<sup>2</sup> <https://gea.esac.esa.int/archive/>

<sup>3</sup> <http://www.cfht.hawaii.edu/Instruments/Filters/wircam.html>

<sup>4</sup> <http://www.cadc-ccda.hia-ihp.nrc-cnrc.gc.ca/en/cfht/>

<sup>5</sup> <http://www.astro.wisc.edu/sirtf/glimpse360/>

**Table 4.** Details of the spectroscopically observed stars.

Star ID	R.A. (J2000) (h:m:s)	Decl. (J2000) (d:m:s)	Spectral Type	$J$ (mag)	$H$ (mag)	$K$ (mag)	Spectroscopic $A_V$ (mag)	Distance Modulus (9)	Distance (pc) (10)	Distance from <i>Gaia</i> (pc) (11)	Remarks
(1)	(2)	(3)	(4)	(5)	(6)	(7)	(8)	(9)	(10)	(11)	
1	05:52:08.13	+27:03:55.64	K1 V-III	7.977 ± 0.009	7.309 ± 0.057	7.065 ± 0.009	2.38 ± 0.06	...	...	1141 ± 64	Foreground
2	05:52:13.83	+26:59:40.83	K0 V-III	8.709 ± 0.015	8.088 ± 0.019	7.884 ± 0.023	2.12 ± 0.02	...	...	1103 ± 70	Foreground
3	05:51:55.41	+27:01:58.03	B0.5 V	9.155 ± 0.021	9.110 ± 0.025	8.982 ± 0.020	1.80 ± 0.04	11.58 ± 0.05	2076 ± 239	2079 ± 192	Member
4	05:52:30.68	+27:01:01.15	G9 V	10.399 ± 0.019	10.007 ± 0.024	9.868 ± 0.019	0.24 ± 0.03	6.19 ± 0.04	173 ± 16	769 ± 32	Foreground
5	05:52:19.65	+27:01:46.83	G0 V	10.006 ± 0.019	9.383 ± 0.024	9.004 ± 0.017	3.28 ± 0.03	...	...	2764 ± 506	Background

**Notes:**

(1) ID Number of the spectroscopically observed stars.

(2-3) Equatorial coordinates of the stars in degrees.

(4) Spectral types estimated from the spectroscopic observations.

(5-7) Photometric parameters of the stars from 2MASS catalog (Skrutskie et al. 2006).

(8-9) Visual extinction ( $A_V$ ) and distance modulus are calculated from spectral types and infrared photometry.

(10) Spectroscopic distances of the stars.

(11) Distance of the stars from *Gaia* DR2 catalog (Gaia Collaboration et al. 2018).

have taken the nearest one as the preferred match. To match the sources detected from WIRCam *JHK* bands, a matching radius of  $1''$  was used. *JHK*, IRAC, and IPHAS catalogs were matched within a matching radius of  $1''$ . We have adopted the matching radius of  $1''$  to match the sources selected from optical and infrared catalog data.

We have used histogram turn over method to estimate the completeness of our utilized data sets. In general, the completeness limits are calculated from histograms, where the logarithmic distribution of the sources deviates from the linear distribution. The completeness limits for different data sets for the S242 region are  $V = 17.8$  mag,  $J = 18.4$  mag,  $H = 17.6$  mag,  $K = 17.2$  mag,  $[3.6] = 16.8$  mag, and  $[4.5] = 16.4$  mag, respectively. However, there may be several additional factors, such as saturation caused by bright luminous sources, variable reddening, stellar crowding, telescope detection sensitivity, etc., that can constrain the completeness of different data sets (Jose et al. 2013).

### 3. RESULTS

#### 3.1. Spectral Classification of the Spectroscopically Observed Stars

The target stars for spectroscopic observations were selected based on their brightness ( $J < 11$  mag) within the cluster region. The details of observations for each star are listed in Table 1. The flux-calibrated normalized spectra of the observed stars obtained with Grism 7 and 8 are presented in Fig. 3.

Spectral classifications were done by comparison to the spectral indices of Danks & Dennefeld (1994), Kobulnicky et al. (2012), and Hernández et al. (2004), and comparison with the spectral atlas of Jacoby et al. (1984), Walborn & Fitzpatrick (1990), and Torres-Dodgen & Weaver (1993). The classification scheme relied on the marking and utilizing of strong conspicuous features for any spectral range. For early-type stars (B, A, and F), we compared the strength of atomic absorp-

tion lines, such as hydrogen Balmer series ( $H\delta$  44102 Å,  $H\gamma$  44340 Å,  $H\beta$  44861 Å,  $H\alpha$  6563 Å), He I ( $\lambda\lambda$ 5876, 6678, 7065 Å), and He II ( $\lambda\lambda$ 4200, 4541, 4686, 5411, 5720 Å) lines. Whereas for cooler stars like G-type or later than that, different metallic line features such as Mg I triplet ( $\lambda\lambda$ 5167, 5172, 5183 Å), Mg II ( $\lambda\lambda$ 4481, 6347 Å), Ca I ( $\lambda\lambda$ 6122, 6162 Å), and Fe I ( $\lambda\lambda$ 6495, 7749, 7834 Å) are used. We also adopted certain constraints on the specific line features. The absence of He II 5411 Å line in any spectra limits the spectral type to B0.5 or later (Kobulnicky et al. 2012), while the absence of He I 5876 Å constrains the spectral type to later than A0 (Lundquist et al. 2014). Si III 4552 Å and O II 4650 Å show maximum strength at spectral type B0.5 V, and He II 4686 Å is last seen up to types B0.5–B0.7 V (Walborn & Fitzpatrick 1990). The declining strength of C III 4070 Å and O II 4650 Å blends are used as an additional criteria to classify the stars in the spectral range B1–B2 V. He I line strength is maximum for B2 type stars, whereas for later than that Si II 44128–4130 Å and Mg II 44481 Å increase distinctly (Walborn & Fitzpatrick 1990). He I 6678 Å appears strongest at O9 V, before disappearing at B8 V (Danks & Dennefeld 1994). The weak presence of O I 7776 Å is notable at B2 V, strengthens to maximum at A5 V and disappears at G0 V. The appearance of Fe I 6495 Å is evident at A2 V and grows in strength to K0 V (Danks & Dennefeld 1994). The presence of Fe I 7749, 7937 Å in any spectrum is an indication of K dwarfs (Allen & Storm 1995). We also compared the equivalent widths of He II 5411 Å, He I 5876 Å and  $H\alpha$  6563 Å for B-type stars, and Na I ( $\lambda\lambda$ 5890–5896 Å),  $H\alpha$  and Ca II triplet ( $\lambda\lambda$ 8498, 8542, 8662 Å) for later-type stars with the spectral indices of Danks & Dennefeld (1994), Kobulnicky et al. (2012), and Lundquist et al. (2014).

The spectroscopic analysis of the observed sources produced only one massive and early-type star (B0.5 V). Other spectroscopically observed sources were found to

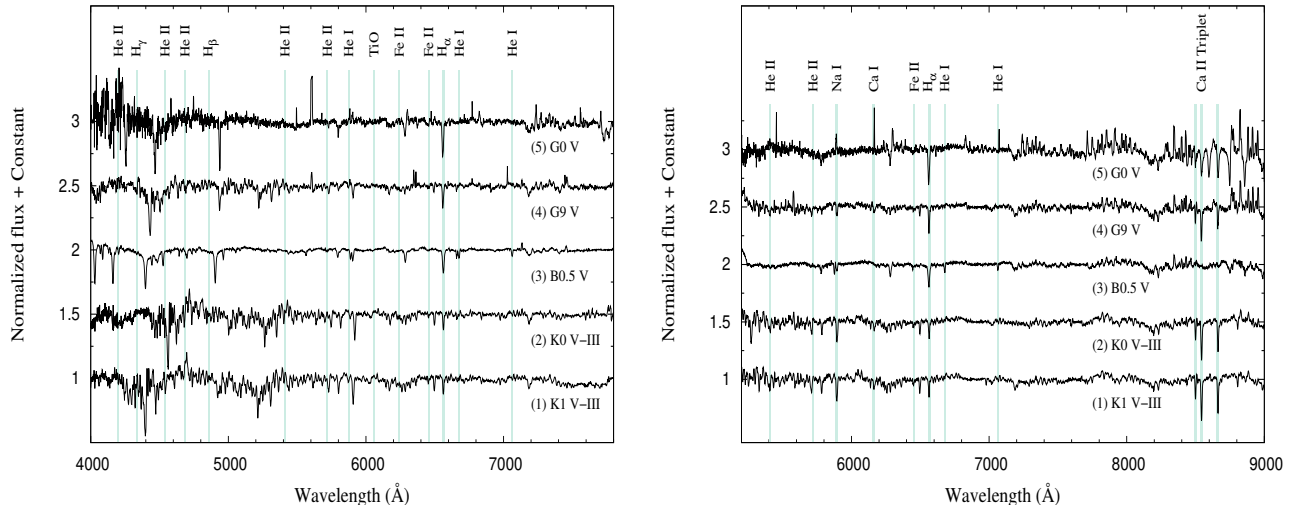


**Figure 3.** Flux-calibrated normalized spectra for the spectroscopically observed stars towards S242, obtained with the 2-m HCT using Grism 7 (left) and Grism 8 (right) respectively. The important emission and absorption line features are marked.

be late-type (either G or K) stars. The star ID 1 shows weaker  $H\alpha$   $\lambda 6563$  Å and  $Na$  I  $\lambda\lambda 5893, 8195$  Å absorption features, presence of  $Fe$  I  $\lambda\lambda 6495, 7747, 7834$  Å and  $Ca$  II triplet  $\lambda\lambda 8498, 8542, 8662$  Å indicative of an early-K type star (K1 V-III). The star ID 2 is classified as K0 V-III, from similar diagnostic as ID 1. The spectrum of star ID 3 shows strong  $He$  I  $\lambda 5876$  Å and  $H\alpha$  absorption feature along with the presence of  $He$  II  $\lambda 4200$  Å and  $He$  I  $\lambda\lambda 6678, 7065$  Å lines. As no signature of  $He$  II  $\lambda 5411$  Å was detected from the spectrum, we categorized the star as B0.5 V spectral type. The stars ID 4 and 5 were classified as G9 V and G0 V type, respectively, for showing weak and narrow  $H\alpha$  absorption features and presence of  $Mg$  I triplet at  $\lambda\lambda 5167, 5172, 5183$  Å. We designated the stars with luminosity class V/III, as their spectral resemblance with the main-sequence/giants are better than super-giants. Also in some cases it was difficult to properly distinguish between the main-sequence and the giant stars. Based on the low-resolution spectroscopy, an uncertainty of  $\pm 1$  spectral subtype for early-type stars up to F- and  $\pm 3$  subtype for G-type and later stars is expected. The photometric and spectroscopic details of the five observed stars are tabulated in Table 4.

### 3.2. Reddening and Membership of the Spectroscopically Observed Stars

Membership estimation of the observed stars toward a cluster region is a crucial step to quantify the essential cluster parameters. The relevant parameters used to ascertain the spectrophotometric distances for each star are listed in Table 4. We used the spectral types and infrared photometry ( $J$ ,  $H$ , and  $K$ ) to determine the distances of the spectroscopically observed bright

sources (Dutta et al. 2015). We have estimated the spectroscopic  $A_V$  of individual sources, using the relation  $E(J - H) = (J - H) - (J - H)_0$ , and similar relations simultaneously for other two bands, where  $(J - H)$  is the observed color and  $(J - H)_0$  being the intrinsic color. The intrinsic distance modulus ( $J_0 - M_J$ ), ( $H_0 - M_H$ ), and ( $K_0 - M_K$ ) were calculated from reddening  $A_V$ , absolute ( $M_J, M_H, M_K$ ) and observed ( $J, H, K$ ) magnitudes. The intrinsic values of magnitudes and colors were taken from Pecaut & Mamajek (2013). The intrinsic distance modulus of star ID 3 was calculated as  $11.58 \pm 0.05$  mag, which corresponds to a distance of  $2.08 \pm 0.24$  kpc. Additionally from the *Gaia* DR2 catalog, the distance of the source is derived as  $2.08 \pm 0.19$  kpc, which is in close agreement with our estimated spectrophotometric distance. Out of the five spectroscopically observed stars, we assigned BD+26 980 (star ID 3) of spectral type B0.5 V, a massive member of the cluster. Others are either foreground or background stars as mentioned in Table 4.

Fig. 4 shows the distribution of sources detected from the observed optical photometry toward S242 in the  $V/(B - V)$  and  $V/(V - I)$  color-magnitude (CM) diagrams. The black filled circles represent the sources with photometric uncertainty  $< 0.1$  mag and gray filled circles are those with photometric uncertainty higher than this. The spectroscopically observed stars are numbered and marked with red circles. The blue solid lines represent the locus of the zero-age main sequence (ZAMS) taken from Girardi et al. (2002) and corrected for the cluster distance of 2.08 kpc, and reddening  $E(B - V) = 0.56$  and  $E(V - I) = 0.70$  mag [ $E(B - V)/E(V - I) = 0.794$ ; Cohen et al. 1981]. In order to shift the ZAMS, we

**Table 5.** Photometric catalog of optically observed point sources toward the S242 region. The complete catalog is available in the electronic version.

Sl. No.	R.A. (J2000) (deg)	Decl. (J2000) (deg)	$V$ (mag)	$B - V$ (mag)	$V - I$ (mag)	$J$ (mag)	$H$ (mag)	$K$ (mag)	[3.6] $\mu\text{m}$ (mag)	[4.5] $\mu\text{m}$ (mag)
(1)	(2)	(3)	(4)	(5)	(6)	(7)	(8)	(9)	(10)	(11)
1	87.930710	27.056652	14.280 $\pm$ 0.004	1.195 $\pm$ 0.009	1.242 $\pm$ 0.005	12.028 $\pm$ 0.021	11.585 $\pm$ 0.027	11.423 $\pm$ 0.023	11.403 $\pm$ 0.044	11.309 $\pm$ 0.025
2	87.980881	27.032787	10.128 $\pm$ 0.025	0.483 $\pm$ 0.025	0.514 $\pm$ 0.025	9.155 $\pm$ 0.021	9.110 $\pm$ 0.025	8.982 $\pm$ 0.020	8.949 $\pm$ 0.034	8.934 $\pm$ 0.028
3	87.983437	27.020210	16.588 $\pm$ 0.011	1.577 $\pm$ 0.031	1.787 $\pm$ 0.013	13.666 $\pm$ 0.019	12.969 $\pm$ 0.025	12.748 $\pm$ 0.025	12.658 $\pm$ 0.036	12.671 $\pm$ 0.036
4	87.959221	27.028023	17.532 $\pm$ 0.019	1.244 $\pm$ 0.068	1.232 $\pm$ 0.031	15.308 $\pm$ 0.036	14.780 $\pm$ 0.050	14.596 $\pm$ 0.073	14.434 $\pm$ 0.042	14.448 $\pm$ 0.065
5	87.957176	27.040668	15.740 $\pm$ 0.005	0.918 $\pm$ 0.011	1.019 $\pm$ 0.010	13.929 $\pm$ 0.023	13.515 $\pm$ 0.025	13.420 $\pm$ 0.030	13.271 $\pm$ 0.043	13.291 $\pm$ 0.040

**Notes:**

- (1) Serial Number of sources.  
(2-3) Equatorial coordinates of sources in degrees.  
(4-6) Photometric magnitudes, colors, and their errors from DFOT (Sagar et al. 2012).  
(7-9) Photometric catalog either from WIRCam (Puget et al. 2004) or 2MASS PSC (Skrutskie et al. 2006).  
(10-11) Photometric catalog from *Spitzer* IRAC (Fazio et al. 2004).

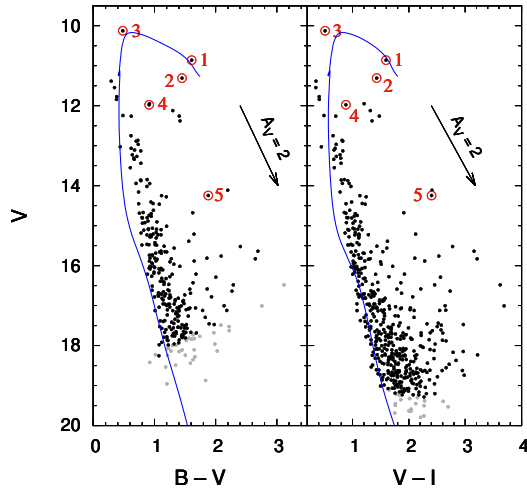


**Figure 4.** Distribution of sources from optical photometry in the CM diagrams. Spectroscopically observed sources are numbered and marked with red circles. The ZAMS from Girardi et al. (2002), corrected for the cluster distance of 2.08 kpc and reddening  $E(B - V) = 0.56$  mag and  $E(V - I) = 0.70$  mag (Table 4), is shown with blue solid lines.

used the extinction  $A_V = 1.8$  mag (Table 4) of the main illuminating source BD+26 980 of the region. The photometric catalog of optically observed point sources toward the S242 region is tabulated in Table 5. A total of 503 sources was detected at least in  $B$ ,  $V$ , or  $I$  band with a limiting magnitude of  $V \sim 19.4$  mag. We obtained a total of 291 sources having counterparts in all the three  $B$ ,  $V$ , and  $I$  bands, within a  $18' \times 18'$  sky area. Although the spatial variation of extinction can be non-uniform throughout the region. There may be several causes for the broad distribution of sources in the CM diagrams, such as variable reddening, presence of field stars, binaries, and peculiar stars. However it is difficult to differentiate the cluster members and field stars from these diagrams.

### 3.3. Extinction Map Toward the S242 Region

Discriminating embedded young stars in clusters from field stars is a salient feature in the study of young stellar distributions of interest. Young cluster environments are rich with dust, reducing the density of background stellar contamination (Gutermuth et al. 2005). Often the nonuniform distribution of dust in these environments makes it far more challenging to get a proper census of detectable background stars (Gutermuth et al. 2005). In general, the distribution of dust in a cloud can be traced by measurements of the extinction of background starlight produced by the cloud (Lada et al. 1994). In order to map the extinction throughout the S242 region, we used  $H$  and  $K$  photometry from the 2MASS catalog with photometric uncertainty  $< 0.1$  mag. Since our target area is not completely covered with WIRCam photometry, we used 2MASS catalog to generate the map. The  $A_K$  values were derived from  $(H - K)$  colors, following the method outlined in more detail by Gutermuth et al. (2005). In brief, we divided the region of our interest into uniform grids of size  $15'' \times 15''$ . We have taken 20 nearest neighbor sources from the center of each grid to calculate the mean and standard deviation of  $(H - K)$  color for each grid, excluding the sources whose  $(H - K)$  values deviated  $3\sigma$  from the mean value. The mean  $(H - K)$  color for each grid were converted to  $A_K$ , using the reddening law  $A_K = 1.82 \times [(H - K)_{obs} - (H - K)_{int}]$  from Flaherty et al. (2007). The average intrinsic color  $(H - K)_{int}$  of the background population was taken into account to accurately characterize the distribution of extinction toward the region. The  $(H - K)_{int}$  color was measured to be 0.2 mag using a nearby unextincted region ( $\alpha_{(2000)} = 05^{\text{h}}51^{\text{m}}54^{\text{s}}$ ,  $\delta_{(2000)} = +28^{\circ}01'54''$ ) of the sky from 2MASS catalog. The control field was chosen  $\sim 1^\circ$  away toward the north of S242. In an attempt to reduce the contribution from embedded young stars, only nonexcess infrared sources were used to generate the extinction map. The final extinction map has an angular resolution of  $15''$  and is sensitive down to  $A_V \sim 17.8$  mag. It is to be noted that the resolution and sensitivity of the map are a function of grid size and number



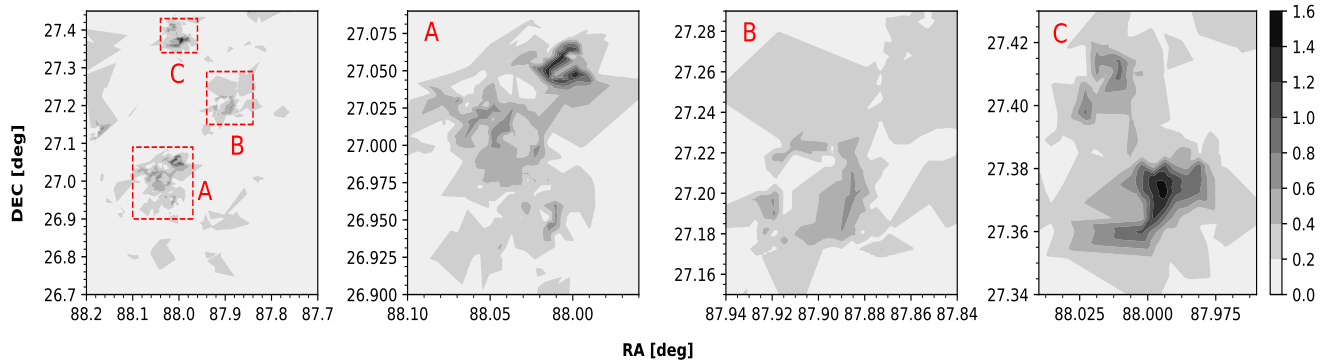


**Figure 5.** The  $K$ -band extinction map generated with  $(H - K)$  colors from the 2MASS catalog. The color bar shows the variation of  $A_K$  for all the plots. The zoomed-in view of the three subregions (Section 3.3) is also shown.

of nearest neighbor sources used. To select the suitable grid size and number of nearest neighbor sources, we performed a series of iterations and found the grid size of  $\sim 15''$  and nearest neighbor source  $\sim 20$  are a good compromise between the sensitivity and signal-to-noise ratio of the extinction map. If the grid size was doubled ( $30''$ ), the sensitivity dropped to  $A_V \sim 1$  mag.

The variation of extinction ( $A_K$ ) throughout the S242 region is shown in the Fig. 5. The extinction shows a highly nonuniform structure throughout the region. In the map, three distinct and isolated extinction peaks are prominent. They are categorized into three subregions ‘A’, ‘B’ and ‘C’ and their zoomed-in distributions are shown in Fig. 5. The subregion ‘C’ suffers with highest value of extinction  $A_V = 17.2$  mag ( $A_K = 1.5$  mag); (Cohen et al. 1981), while the subregion ‘A’ has a maximum extinction of  $A_V = 16.1$  mag ( $A_K = 1.4$  mag). The subregion ‘B’ shows a modest distribution of extinction, with a maximum value of  $A_V = 7.4$  mag ( $A_K = 0.7$  mag). Among the three extinction complexes, subregions ‘A’ and ‘C’ are the highly extinguished regions. These two regions are supposed to be the dominant sites for the next generation star formation. Subregion ‘B’ is supposed to be relatively evolved or its association with molecular clouds is significantly less compared with ‘A’ and ‘C’. Throughout the region the extinction varies from  $A_V = 1.3$ – $17.2$  mag ( $A_K = 0.1$ – $1.5$  mag), and the average value of extinction is  $A_V = 3.1$  mag ( $A_K = 0.3$  mag) with a standard deviation of  $A_V \sim 0.8$  mag ( $A_K \sim 0.07$  mag). Although, this analysis is limited by sensitivity of the 2MASS survey. The derived extinction can also be underestimated due to the lack of detection of a sufficient number of background stars in the heavily extinguished areas.

### 3.4. Identification and Classification of YSOs

The infrared color-color (CC) space analysis is an efficient tool to identify and characterize the YSOs (Lada

& Adams 1992). The YSOs show excess infrared emission due to the presence of circumstellar disks and envelopes and thus occupy certain locations in the infrared CC diagrams. We used IRAC and  $JHK$  colors to classify the young sources toward the S242 region. We adopted the IRAC [3.6] and [4.5]  $\mu\text{m}$  along with the WIRCam  $H$  and  $K$  bands photometry to categorize the pre-main-sequence (PMS) populations using the methods described in Gutermuth et al. (2009). Though the infrared excess emission is an essential and powerful membership diagnostic for young and embedded sources, this method also suffers from many potential contaminants. The dominant limitations arise from the extragalactic sources like star-forming galaxies, narrow- and broad-line active galactic nuclei (AGNs), as well as polycyclic aromatic hydrocarbon (PAH) emission excited by young and high-mass stars (Gutermuth et al. 2008). We used  $JHK$  photometry from the WIRCam and the 2MASS catalog as an additional tool for further classification of sources that lack higher wavelength IRAC data. Since a majority of the  $H\alpha$  emitters toward H II regions are considered as classical T Tauri stars (CTTs; Meyer et al. 1997), due to the presence of hot and infalling gas accreting from circumstellar disks (Barentsen et al. 2011), we used the IPHAS photometry as an additional criteria to detect the young stars showing  $H\alpha$  emission.

#### 3.4.1. Selection of YSOs from IRAC Data

Since the S242 region was observed during the *Spitzer* Warm Mission (Hora et al. 2012), the MIR catalog is restricted to [3.6] and [4.5]  $\mu\text{m}$  bands only. Hence, we used IRAC [3.6] and [4.5]  $\mu\text{m}$  along with WIRCam  $H$  and  $K$  photometry to effectively identify and classify the YSOs. The YSOs in an embedded star cluster suffer high spatially variable extinction due to the presence of natal molecular cloud clumps. We used dereddened IRAC and WIRCam colors by measuring the line-of sight ex-

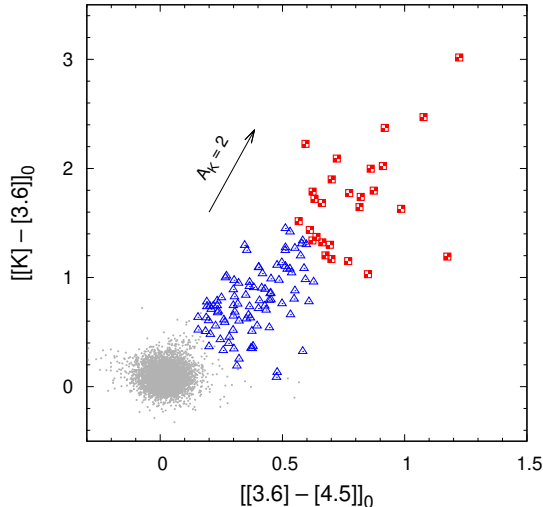


**Figure 6.** Classification of Class I and Class II sources from the dereddened CC diagram using  $H$ ,  $K$ ,  $[3.6] \mu\text{m}$ , and  $[4.5] \mu\text{m}$  photometry, after removing the contaminants. Class I and Class II sources are represented by red squares and blue triangles, respectively. Reddening vector for  $A_K = 2$  mag is indicated by the black arrow.

inction of each source, following the Gutermuth et al. (2009) classification scheme.

Field star contamination was removed by generating the extinction map (Section 3.3) throughout the region using the 2MASS catalog. To compute the dereddened colors ( $[[3.6] - [4.5]]_0$  and  $[[K] - [3.6]]_0$ ) of each source, the extinction of the nearest grid from that source was taken into account. We have identified the YSOs from the dereddened color space using the criteria given by Gutermuth et al. (2009), after removing several non-stellar contaminants. An additional brightness cut on the dereddened  $[3.6] \mu\text{m}$  photometry was applied to reduce the inclusion of dim extragalactic contaminants with Class II sources must have  $[3.6]_0 < 14.5$  mag and Class I sources satisfy  $[3.6]_0 < 15$  mag (Gutermuth et al. 2009). We accomplished a total of 27 Class I and 96 Class II sources for the S242 region using IRAC and WIRCam data. Fig. 6 depicts the distribution of Class I (red squares) and Class II (blue triangles) sources in addition to nonexcess field stars (gray dots) in the dereddened CC space. The reddening vector for  $A_K = 2$  mag is also indicated in the diagram, whereas the color excess ratios were obtained from Flaherty et al. (2007).

#### 3.4.2. Additional YSOs from WIRCam and 2MASS Photometry

We used infrared  $JHK$  photometry as an additional selection criteria to distinguish further young objects associated with the molecular dust and cloud. Fig. 7 shows the distribution of identified YSOs in the  $(J -$

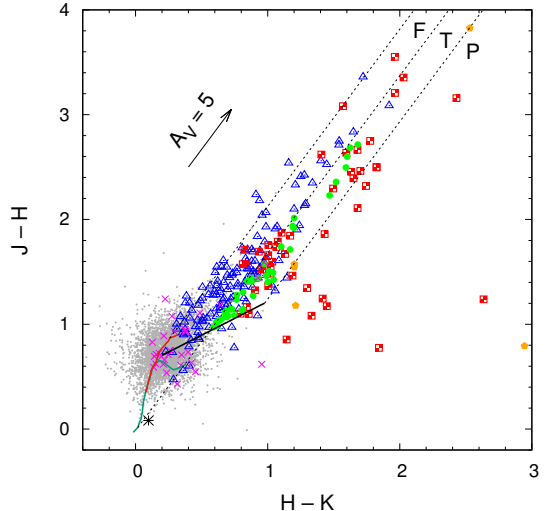


**Figure 7.** The distribution of YSOs in the NIR CC diagram. The locus of points for unreddened dwarfs and giants are represented by solid green and red lines, respectively. The black solid line indicates the CTTs locus. Red and blue symbols are same as in Fig. 6. The green circle and orange star symbols represent the additional YSOs selected from this diagram. The magenta crosses are the  $H\alpha$  emission line sources selected from IPHAS photometry (Section 3.5). The main exciting source BD+26 980 is indicated by a black star symbol and located toward the base of main-sequence locus.

$H)/(H - K)$  CC diagram throughout the S242 region. This method is an efficient tool to distinguish the heavily reddened stars having intrinsic infrared excess from those showing normal unreddened photospheric colors (Lada & Adams 1992). The locus of points corresponding to unreddened main-sequence stars and giants is taken from Bessell & Brett (1988) and represented by green and red solid lines in Fig. 7. The black solid line indicates the CTTs locus, taken from Meyer et al. (1997). All the photometric magnitudes were converted to the CIT (Elias et al. 1982) system using the relations from Carpenter (2001). The three parallel dashed lines show the reddening vectors (Lada & Adams 1992). The reddening laws ( $A_J/A_V = 0.265$ ,  $A_H/A_V = 0.155$ , and  $A_K/A_V = 0.090$ ) were taken from Cohen et al. (1981).

The NIR CC space is divided into three regions, i.e. ‘F’, ‘T’ and ‘P’ (Lada & Adams 1992; Ojha et al. 2004; Dutta et al. 2015). The sources located within the ‘F’ region are bounded by the reddening vectors drawn from the unreddened dwarf and giant branches. They have colors similar to normal stellar photospheric sources and are likely to be field stars (main-sequence stars or giants), weak-line T Tauri stars (WTTs), or Class III sources having no or less infrared excess. The ‘T’ region lies within the reddening vectors projected from main-sequence and CTTs loci. They are considered to

be CTTs or Class II sources characterized by the presence of excess infrared emission. The ‘P’ region is located outward to the reddening vector drawn from the points of CTTs locus and the sources show color redder than those in ‘F’. These sources are most likely Class I objects and show large infrared excess emission due to the heated inner envelopes/atmospheres of the protostars. Although the usefulness of this method to precisely determine the nature of the YSOs is under certain potential limitations (Lada & Adams 1992).

Using the NIR  $JHK$  photometry from WIRCam and 2MASS catalog, we have identified 9 Class I and 59 Class II sources toward S242, with given restrictions on photometric uncertainties  $< 0.1$  mag. Among the 68 YSOs selected from  $(J - H)/(H - K)$  CC diagram, 21 sources were previously categorized from IRAC colors (Section 3.4.1). Effectively, we obtained 6 and 41 additional YSOs having colors consistent with Class I and Class II, respectively, using the  $JHK$  photometry. The S242 region is enriched with 33 Class I and 137 Class II young objects derived from the combined results of IRAC, WIRCam, and 2MASS photometry. The membership status of the YSOs are further confirmed with the inclusion of distances from the *Gaia* DR2 catalog. The distances of the young objects were derived from the available parallax measurements. The photometric and astrometric parameters of the selected YSOs are presented in the Table 6. While a total of 170 young sources were detected from the infrared photometry, only 28 sources (16.47%) were supplemented with distances available from the *Gaia* DR2. However we do not attempt to further distinguish the Class III objects from WTTs or field population from only this diagram, as this may lead to wrong interpretation (Dutta et al. 2015).

### 3.5. $H\alpha$ Emitting Sources from Slitless Spectroscopy and IPHAS Photometry

Using the slitless spectroscopic data from the HCT, we have visually identified a total of three sources that show counterparts in  $H\alpha$  emission. All the three sources are depicted as blue crosses in the CC diagram (Fig. 8) and were also detected from IPHAS photometry. No extra sources were found from the slitless spectroscopy.

The IPHAS survey provides photometry of fainter emission line objects up to  $r = 20.5$ , and  $i$  and  $H\alpha = 19.5$  mag with photometric uncertainty limited to 0.1 mag (Barentsen et al. 2014). Fig. 8 shows the  $(r - i/r - H\alpha)$  CC diagram for the sources detected in the IPHAS catalog toward the S242 region. The solid and dashed blue lines represent the unreddened main-sequence and the expected position of unreddened main-

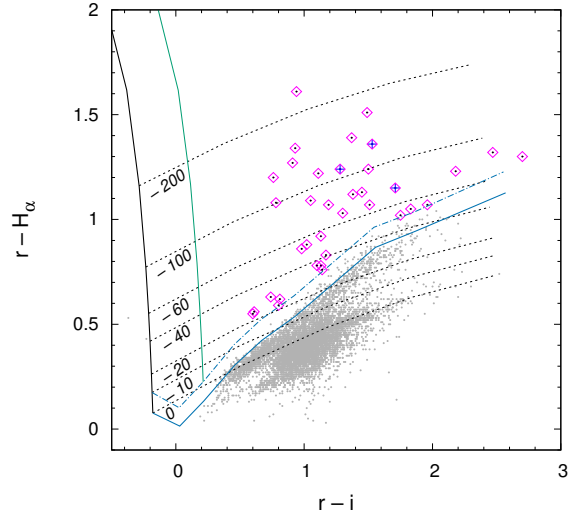


**Figure 8.** The sources detected in IPHAS photometry are shown in the CC diagram. Blue crosses are the sources detected from slitless spectroscopy and magenta boxes are those selected from IPHAS photometry, with prominent  $H\alpha$  emission. Sources with no significant  $H\alpha$  emission lines are depicted as gray dots.

sequence stars with  $H\alpha$  emission line strengths of equivalent width (EW) =  $-10 \text{ \AA}$ . The nearly vertical solid black and green lines show the trend for an unreddened Rayleigh-Jeans continuum and an unreddened optically thick disk continuum (Barentsen et al. 2014; Dutta et al. 2015), respectively. Whereas the black broken lines are predicted lines of constant net emission EW. The reliable sources are selected by applying the quality criteria of  $r < 20$  mag and photometric uncertainty  $< 0.1$  mag in all three bands in IPHAS DR2. A total of 36  $H\alpha$  emission line stars was selected as lying above the dashed blue line at the level of  $3\sigma$ , i.e. the distance between the selected objects and the dashed blue line is larger than three times the average uncertainty in their  $(r - H\alpha)$  color (Barentsen et al. 2014). These candidate  $H\alpha$  emitters are represented by magenta boxes in the CC diagram. The majority of the  $H\alpha$  emitters toward a H II region are likely to be CTTs (Barentsen et al. 2011, 2014). Among the 36  $H\alpha$  emitting objects, 5 sources show infrared counterparts and are classified as Class II sources either from IRAC or  $JHK$  colors. The photometric catalog of the  $H\alpha$  emitting sources is detailed in Table 7.

## 4. DISCUSSION

### 4.1. Spectral Nature of YSOs from NIR CM Diagram

The NIR CM ( $H - K$  versus  $K$ ) space serves as a practical tool to estimate the spectral nature of YSOs by incorporating their distribution in the diagram. Fig. 9

**Table 6.** Photometric catalog of YSOs toward S242. The complete catalog is available in the electronic version.

Sl. No.	R.A. (J2000) (deg)	Decl. (J2000) (deg)	$g_{P1}$ (mag)	$y_{P1}$ (mag)	$J$ (mag)	$H$ (mag)	$K$ (mag)	[3.6] $\mu\text{m}$ (mag)	[4.5] $\mu\text{m}$ (mag)	Distance (pc)
(1)	(2)	(3)	(4)	(5)	(6)	(7)	(8)	(9)	(10)	(11)
Class I sources										
1	88.050873	26.980659	22.056 ± 0.250	19.045 ± 0.058	17.158 ± 0.031	15.508 ± 0.024	14.647 ± 0.021	12.528 ± 0.054	11.882 ± 0.040	...
2	88.073463	26.780842	19.336 ± 0.003	15.986 ± 0.004	14.647 ± 0.043	17.198 ± 0.080	13.582 ± 0.044	13.373 ± 0.041	13.282 ± 0.036	2203 ± 607
3	88.010284	27.060272	...	...	16.392 ± 0.026	13.475 ± 0.016	11.624 ± 0.026	9.793 ± 0.035	9.006 ± 0.038	...
4	88.039421	27.009676	...	...	18.336 ± 0.073	15.803 ± 0.024	14.082 ± 0.015	12.392 ± 0.060	11.394 ± 0.036	...
5	88.038254	26.996187	...	...	18.521 ± 0.097	15.922 ± 0.023	14.220 ± 0.014	12.907 ± 0.052	12.072 ± 0.049	...
Class II sources										
1	88.045395	27.021883	20.375 ± 0.012	17.074 ± 0.110	14.845 ± 0.015	13.640 ± 0.014	12.956 ± 0.016	12.107 ± 0.044	11.572 ± 0.038	2042 ± 880
2	87.967293	26.984737	20.695 ± 0.053	16.880 ± 0.004	15.073 ± 0.024	13.977 ± 0.025	13.394 ± 0.013	12.775 ± 0.033	12.441 ± 0.035	1158 ± 320
3	87.931961	27.002106	19.653 ± 0.016	16.094 ± 0.004	14.621 ± 0.021	13.553 ± 0.025	13.005 ± 0.014	12.793 ± 0.035	12.402 ± 0.030	3056 ± 1351
4	87.992462	26.981787	21.939 ± 0.089	16.875 ± 0.016	15.129 ± 0.018	13.876 ± 0.016	13.461 ± 0.032	12.808 ± 0.043	12.487 ± 0.033	...
5	88.025650	27.058596	20.403 ± 0.026	15.772 ± 0.009	13.670 ± 0.017	12.012 ± 0.028	10.986 ± 0.020	9.587 ± 0.035	8.965 ± 0.030	...

**Notes:**

- (1) Serial Number of sources.  
(2-3) Equatorial coordinates of sources in degrees.  
(4-5) Photometric magnitudes and their errors from the Pan-STARRS 1 catalog (Chambers et al. 2019).  
(6-8) Photometric catalog either from WIRCam (Puget et al. 2004) or 2MASS PSC (Skrutskie et al. 2006).  
(9-10) Photometric catalog from *Spitzer* IRAC (Fazio et al. 2004).  
(11) Distance of sources from the *Gaia* DR2 catalog (Gaia Collaboration et al. 2018).

**Table 7.** Photometric catalog of H $\alpha$  emitters toward S242. The entire catalog is available in the electronic version.

Sl. No.	R.A. (J2000) (deg)	Decl. (J2000) (deg)	$r$ (mag)	$i$ (mag)	H $\alpha$ (mag)	$J$ (mag)	$H$ (mag)	$K$ (mag)	Distance (pc)	Class I/ Class II
(1)	(2)	(3)	(4)	(5)	(6)	(7)	(8)	(9)	(10)	(11)
1	88.006538	26.959366	18.95 ± 0.04	17.67 ± 0.02	17.71 ± 0.02	17.284 ± 0.183	16.328 ± 0.185	15.913 ± 0.224	1685 ± 821	II
2	87.985306	27.042868	19.55 ± 0.05	18.79 ± 0.05	18.35 ± 0.03	16.081 ± 0.069	15.362 ± 0.088	14.977 ± 0.101	1221 ± 1492	...
3	87.969727	27.047367	18.71 ± 0.03	17.69 ± 0.02	17.83 ± 0.02	15.342 ± 0.031	14.494 ± 0.041	14.336 ± 0.056	...	...
4	88.241554	26.771357	19.54 ± 0.06	18.37 ± 0.03	18.71 ± 0.04	16.507 ± 0.104	15.885 ± 0.122	14.876 ± 0.099	1655 ± 1312	...
5	87.995338	27.029369	18.36 ± 0.02	16.98 ± 0.01	17.24 ± 0.02	16.604 ± 0.100	15.755 ± 0.116	15.670 ± 0.178	735 ± 86	...

**Notes:**

- (1) Serial Number of sources.  
(2-3) Equatorial coordinates of sources in degrees.  
(4-6) Photometric magnitudes and their errors from the IPHAS DR2 source catalog (Barentsen et al. 2014).  
(7-9) Photometric catalog either from WIRCam (Puget et al. 2004) or 2MASS PSC (Skrutskie et al. 2006).  
(10) Distance of sources from the *Gaia* DR2 catalog (Gaia Collaboration et al. 2018).  
(11) Type of class

depicts the YSOs identified from the WIRCam, 2MASS, and IRAC catalogs; H $\alpha$  emitters from the IPHAS photometry, and field population distribution, respectively. The locus of ZAMS (Pecaut & Mamajek 2013), reddened by  $A_V = 0, 5, 10, 20,$  and  $30$  mag and corrected for the cluster distance of 2.08 kpc (taken from Table 4) are represented by nearly vertical lines. The slanting horizontal lines are the reddening vectors corresponding to different spectral types. All the symbols in the figure are same as in Fig. 7. From the diagram, it is apparent that the YSOs show a large variation in spectral type from K6 to B0, with a majority concentrated within G0 to B2. The main illuminating source of the S242 cluster is located toward the reddening vector corresponding to B0 spectral type, as marked by a black star symbol. Earlier the spectral nature of this star was mentioned as B0 V, which is quite consistent with our results, and the spectroscopic analysis also reveals it as a B0.5 V type star. It is prominent that a reasonable amount of YSOs suffer large reddening of about 20 to 30 mag, possibly caused due to the presence of dusty circumstellar envelopes and gaseous environments. So, S242 is a rich stellar cluster, evolving with considerable number of young members

and showing wide span in their spectral variation. The gray dots, representing the sources having no or less infrared excess emission, are primarily field population. A majority of them are concentrated within  $(H - K) < 0.6$  mag.

#### 4.2. Estimation of Average Age of the YSOs

We used Pan-STARRS 1 photometry to diagnose the age spread of the YSOs within the S242 region. Since our observed optical data are not deep enough to detect most of the young sources, we used Pan-STARRS 1 photometry. The magnitude depth of the observed optical photometry is down to  $V \sim 19.4$  mag, whereas Pan-STARRS 1 provides photometry deeper down to  $g_{P1} \sim 22.5$  mag and  $y_{P1} \sim 20.2$  mag for this region. The distribution of YSOs and H $\alpha$  emitting sources in the  $(g_{P1} - y_{P1})$  versus  $g_{P1}$  CM diagram is shown in Fig. 10. The ZAMS and PMS isochrones from Marigo et al. (2017), corrected for the cluster distance of 2.08 kpc, reddening  $E(B - V) = 0.56$  mag (taken from Table 4), and  $E(g_{P1} - y_{P1}) = 1.26$  mag (Schlafly et al. 2016) are overplotted. The evolutionary tracks for various masses are also shown to characterize the mass spectrum of the

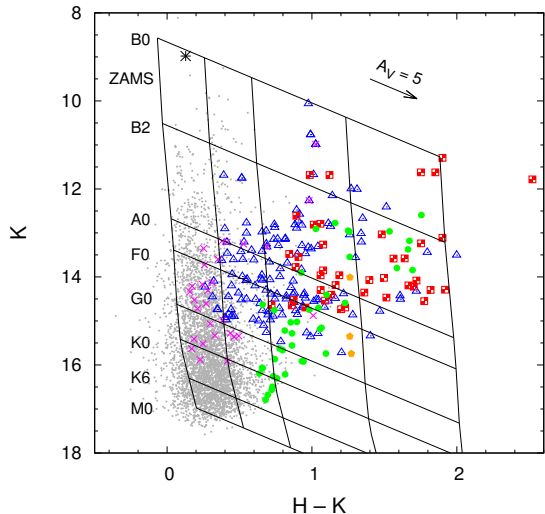


**Figure 9.** The distribution of YSOs selected from infrared catalogs,  $H\alpha$  emitters from IPHAS photometry, and field population toward S242. The nearly vertical lines are the loci of ZAMS (Pecaut & Mamajek 2013) with visual extinction  $A_V = 0, 5, 10, 20,$  and  $30$  mag and shifted for the cluster distance of 2.08 kpc. The slanting horizontal lines represent the reddening vectors corresponding to different spectral types. The symbols used in this figure are the same as in Fig. 7.

YSOs. A notable scatter in the age distribution of the YSO population is observed in Fig. 10. The ages vary between 0.1 Myr and 10 Myr, with a majority indicating an age around 1 Myr. However, our age determination method can be subject to a few limitations: the use of different PMS evolutionary models can yield different ages (Sung, Chun & Bessel 2000), the presence of variable extinction, binaries, and variables may also introduce systematic errors (Herbst et al. 1994; Herbst & Shevchenko 1999). We ascertained an average age of the YSOs as 1 Myr. Most of the  $H\alpha$  emitting sources are relatively evolved compared to the YSOs, as seen from their distribution in the CM diagram. As a larger fraction of the low-mass YSOs lack the reliable photometry, this diagram cannot be used as a suitable tool to estimate mass ranges of the region.

#### 4.3. Mass Distribution of the YSOs from NIR CM Diagram

We used the NIR CM ( $J - H$  versus  $J$ ) diagram to estimate the mass ranges of candidate YSOs toward the S242 region. Since the YSOs show excess emission at longer wavelengths, we used ( $J - H$ ) versus  $J$  diagram in an attempt to reduce the effect of excess emission (Ojha et al. 2004, 2011; Dutta et al. 2015). The NIR CM diagrams allow us to manipulate two fundamental parameters of a cluster, the distance and reddening. The change in distance shifts the isochrones vertically, while

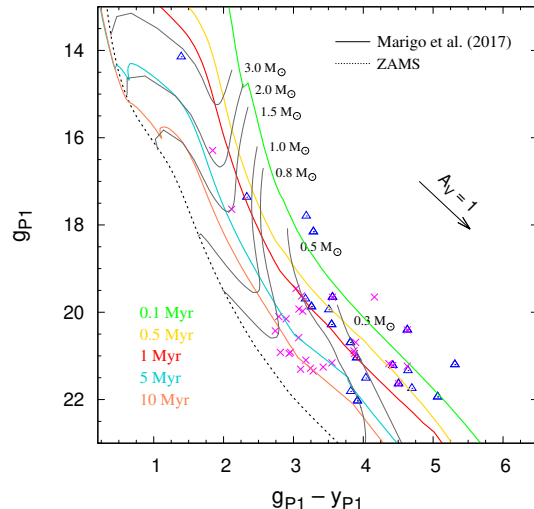


**Figure 10.** Optical/NIR CM diagram showing the distribution of YSOs and  $H\alpha$  emitting sources from the PS1 catalog. The ZAMS and PMS isochrones for ages 0.1, 0.5, 1, 5, and 10 Myr are taken from Marigo et al. (2017). The evolutionary tracks for different masses are also shown. All the isochrones and tracks are corrected for a distance of 2.08 kpc and reddening  $E(B - V) = 0.56$  mag. The source symbols are the same as in Fig. 7.

the parallel slanting lines trace the reddening zones for each extinguished mass vector. Masses were estimated by comparing the distribution of young objects with theoretical PMS isochrones in the diagram. In Fig. 11, the blue solid line presents the loci of ZAMS taken from Girardi et al. (2002) and shifted for the cluster distance of 2.08 kpc. The evolutionary models of PMS isochrones of age 0.1, 1, and 10 Myr are taken from Marigo et al. (2017) and indicated by green, black, and red solid lines. The black dashed lines are the reddening vectors corresponding to different mass tracks, respectively. We used the same symbols as in Fig. 7 to represent the YSOs identified from infrared CC diagrams and  $H\alpha$  emitters from IPHAS photometry. We used an average age of 1 Myr (Section 4.2) to estimate the mass ranges of YSOs. The YSOs show a wide range of variation in their masses with a majority having masses between 0.1 and  $3.0 M_{\odot}$ , as indicated in the figure. It is also observed that the YSOs show larger variation in their color, probably an indication of the combined effect of spatially variable extinction and a weak contribution of excess emission in the  $J$  and  $H$  bands (Ojha et al. 2011). Few of the candidate YSOs are seen to be more massive ( $> 3.0 M_{\odot}$ ) and also located in highly extinguished ( $A_V \sim 10-30$  mag) regions. It is to be noted that estimating the stellar masses from the infrared CM diagrams relies on uncertain ages and different distances to the objects. The ambiguity is even more severe among the massive members (early

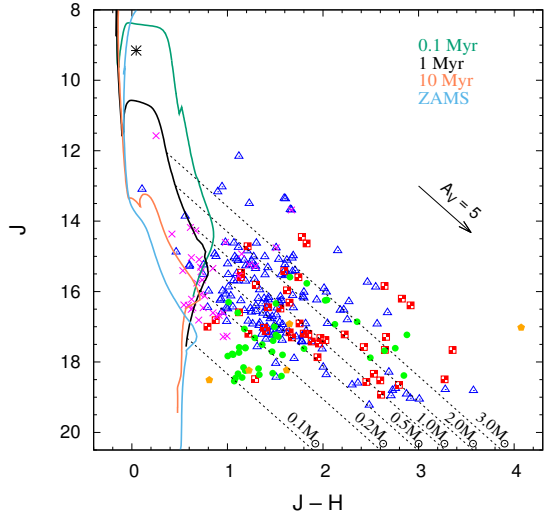


**Figure 11.** The mass spectrum of the YSOs toward S242 is shown in the NIR CM diagram. The locus of ZAMS (Girardi et al. 2002) and PMS isochrones of ages 0.1 Myr, 1 Myr, and 10 Myr (Marigo et al. 2017) are indicated by blue, green, black, and red solid lines, respectively. The reddening vectors corresponding to different mass values are represented by black dashed lines. All other symbols are the same as in Fig. 7.

B-type stars). Because the stellar mass can vary significantly when estimated from a 1 Myr PMS isochrone compared to the main-sequence isochrones of a younger age. Therefore, estimating the parameters for the massive members was difficult. Also, there can be several other causes which put constraints on this method, such as the use of separate PMS isochrones, binarity, and variable extinction (Hillenbrand et al. 2008).

#### 4.4. Spatial Distribution of the PMS Population

The spatial variation of the embedded young stellar population is a footprint of how star formation has progressed throughout space and time in a given region. Fig. 12 manifests the distribution of Class I (red circles), Class II (blue triangles), and  $H\alpha$  emission line (green boxes) sources, overlaid on the *WISE*  $W1$   $3.4 \mu\text{m}$  mosaic image. The location of the main ionizing star BD+26980 is marked by a black star symbol. The FOV of DFOT optical ( $18' \times 18'$ ), WIRCam NIR ( $29' \times 26'$ ), and other archival photometric catalogs (2MASS, *Spitzer*, *Gaia* DR2, IPHAS) for a radius of  $25'$  are indicated in the figure. A noticeable number of the PMS populations are preferentially concentrated around the central core region. A majority of the YSOs are seen to be spatially aligned along an elongated filamentary structure (EFS). From the distribution of young stellar candidates, the spatial extent of the elongated structure is estimated as  $\sim 43'$  (26 pc). Using the  $^{13}\text{CO}$  molecular

line data, Dewangan et al. (2017) also reported the presence of an EFS of length  $\sim 25$  pc and average width  $\sim 1.3$  pc. A significant number of the Class I sources have formed two discrete groups, one at the central region and another at the northern end of the long scale structure. While Class II type sources also show a similar grouping as Class I sources along with a nice positional coincidence with the long scale feature. The three peak extinction complexes, marked by ‘A’, ‘B’ and ‘C’ (see Section 3.3 for details) are shown by red dashed boxes in the diagram. The prominent clustering of the young populations are nicely match the extinction complexes. The spatial distribution of YSOs along the filamentary-like extinction structure indicates that ongoing star formation is likely occurring toward the cluster.

The number of YSOs in each class is useful to estimate the relative age of the subclusters in a young region (Hatchell et al. 2007; Gutermuth et al. 2009; Saral et al. 2015). We used the ratio of number of Class I sources to the number of Class II sources to interpret the evolutionary status of the star-forming region. Since Class I objects represent the earlier phase of star formation compared to Class II sources, the Class I/II ratio serves as a proxy to estimate the relative age of the subclusters (Chavarría et al. 2008). The ratio of Class I/II for the subregions ‘A’ and ‘C’ are obtained as 0.31 in both the cases. Whereas, for subregion ‘B’, the ratio is quite low: 0.08. Using a MIR survey of 36 young and active star-forming clusters, Gutermuth et al. (2009) estimated the median ratio of Class I/II to be 0.27. For the overall S242 region, the ratio is obtained as  $\sim 0.25$ , which is in close proximity to the value derived by Gutermuth et al. (2009). Studying a nearby star forming complex, Chavarría et al. (2008) has shown the ratio of Class I/II to vary between 0.31 and 0.78. Beerer et al. (2010) presented the Class I/II ratio to range from 0.05 to 0.78 for 13 young clusters. Jose et al. (2013) evaluated the ratio to vary between 0.13 and 0.54 for the different subregions of a large H II region. The Class I/II ratio is a function of the evolutionary stage of the complex, where the higher ratio indicates a younger cluster (Chavarría et al. 2008; Beerer et al. 2010). The ratio of Class I/II suggests that the subregions ‘A’ and ‘C’ are the locations of the youngest population for the region and the sources in these groups are evolving almost on a similar timescale. In general, it is predicted from the spatial distribution of the YSOs and the Class I/II ratio that the S242 region is in its early stage of star formation. Comparing the ratio of Class I/II with the earlier reports (Chavarría et al. 2008; Beerer et al. 2010; Jose et al. 2013; Saral et al. 2017), the average age of the young members in the S242 region is estimated around

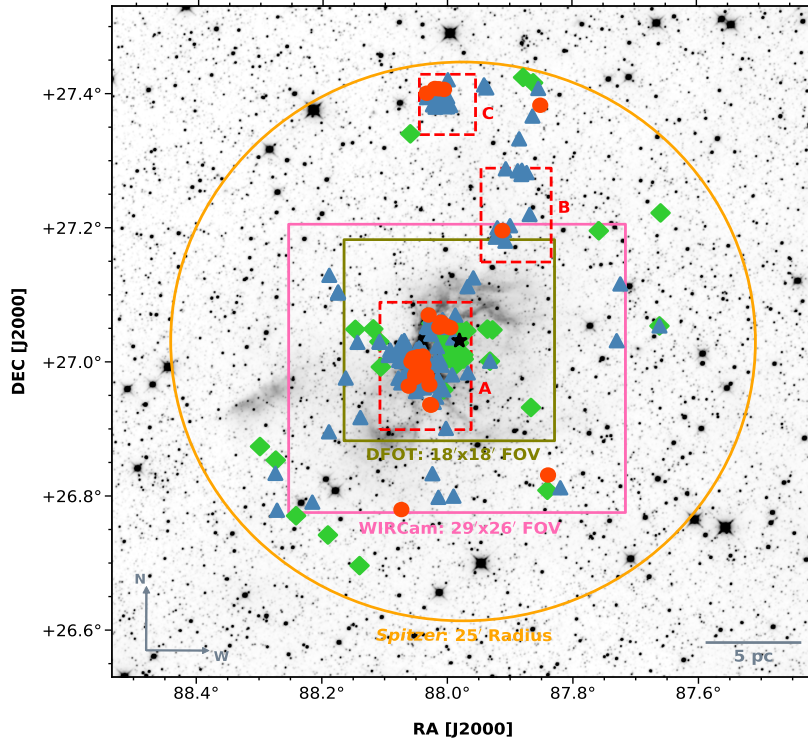


**Figure 12.** Spatial distribution of the PMS sources, overplotted on the *WISE* *W1*  $3.4 \mu\text{m}$  mosaic image. The Class I, Class II, and  $\text{H}\alpha$  emitting sources are represented by red circles, blue triangles, and green boxes, respectively. The main ionizing source BD+26 980 is represented by a black star symbol. The FOV for different observed and archival catalogs (see Section 4.4 for details) are indicated.

1 Myr. Although, as the subregions ‘A’ and ‘C’ suffer the highest extinction, it may cause undercounting due to the undetectable background stars. Also limitations may occur with distance of the sources and detection sensitivity of the instruments.

## 5. SUMMARY AND CONCLUSIONS

In this work, we report a multiwavelength survey of the stellar content and its characterization toward the S242 region, using combined observed and archival data sets. The key results are summarized as follows:

1. The slit spectroscopic results confirmed classification of the main ionizing source BD+26 980 as a massive and early-type (B0.5 V) star of the region. The spectrophotometric distance of the star is estimated as  $2.08 \pm 0.24$  kpc, confirming its membership with the region. *Gaia* DR2 also provides a similar distance ( $2.08 \pm 0.19$  kpc) for the star. The rest of the spectroscopically observed sources are late-type (either G or K) foreground or background stars.
2. The *K*-band extinction map was generated using a nearest neighborhood technique and the average extinction within the region was estimated as  $A_V \sim 3.1$  mag. From the extinction map (diameter  $\sim 50'$ ), three distinct extinction peaks were identified toward the region for the first time in this work and their corresponding consequences were discussed.
3. Using the infrared color excess from the combined photometry of NIR (WIRCam and 2MASS) and MIR (*Spitzer*) catalogs, a total of 33 Class I and 137 Class II objects were detected within the selected area. Thus the S242 cluster appears as a prominent star-forming region, where a significant number of young stellar populations are found to be forming and evolving together.
4. The  $\text{H}\alpha$  emission line objects were detected from IPHAS photometry and slitless spectroscopic observations. We have identified 36  $\text{H}\alpha$  emitting sources, which are bonafide young objects toward the S242 region.
5. Using parallaxes from the *Gaia* DR2 catalog, the membership status of the classified young population was revealed.
6. Using the Pan-STARRS 1 deep photometry, an average age of the YSOs was estimated as 1 Myr toward the region. From the infrared CM diagram,

the masses of the young populations were found to vary between 0.1 and  $3.0 M_{\odot}$ .

7. The cospatial distribution of the young stellar population and the filamentary-like extinction structure is an indication of recent star formation activity within the region. An EFS of length  $\sim 25$  pc is estimated from the projected distribution of the PMS sources. The relatively high fraction ( $\sim 0.25$ ) of Class I to Class II objects suggests that the YSO population is in a very early stage ( $\sim 1$  Myr) of evolution.

#### ACKNOWLEDGEMENTS

We thank the anonymous referee for a critical reading of the manuscript and for providing several useful comments and suggestions that significantly improved the scientific content of the paper. This research work was supported by the S. N. Bose National Centre for Basic Sciences, under the Department of Science and Technology, Government of India. This publication makes use of the observational data from WIRCam, a joint project of CFHT. This work makes use of data prod-

ucts from the 2MASS, which is a joint project of the University of Massachusetts and the Infrared Processing and Analysis Center/California Institute of Technology. This work is based [in part] on observations made with the *Spitzer Space Telescope*, which is operated by the Jet Propulsion Laboratory. Archival data are used from Pan-STARRS 1 surveys, operated by the University of Hawaii. This work makes use of the data from IPHAS catalog operated by the Isaac Newton Group of Telescopes. This work presents results from the European Space Agency space mission *Gaia*. *Gaia* data are being processed by the *Gaia* Data Processing and Analysis Consortium (DPAC). We are thankful to the staff of the Indian Astronomical Observatory, Hanle and Centre for Research and Education in Science & Technology, Hosakote for providing the observational facilities from HCT, operated by the Indian Institute of Astrophysics, Bangalore. The authors are thankful to the staff and members of DFOT, operated by Aryabhata Research Institute of Observational Sciences, Nainital.

*Software:* IRAF (Tody 1986, 1993), DAOFIND (Stetson 1992), DAOPHOT (Stetson 1992), ALLSTAR routine (Stetson 1987), SIMPLE (Wang et al. 2010)

#### REFERENCES

- Adams F. C., Porszkow E. M., Fatuzzo M., et al., 2006, *ApJ*, 641, 504
- Adams F. C., 2010, *ARA&A*, 48, 47
- Allen L. E., Storm K. M., 1995, *AJ*, 109, 1379
- Anderson L. D., Bania T. M., Balser D. S., et al., 2014, *ApJS*, 212, 1
- Barentsen G., Farnhill H. J., Drew J. E., et al. 2014, *MNRAS*, 444, 3230
- Barentsen G., Vink J. S., Drew J. E., et al., 2011, *MNRAS*, 415, 103
- Beerer I. M., Koenig X. P., Hora J. L., et al., 2010, *ApJ*, 720, 679
- Bessell M. & Brett J. M., 1988, *PASP*, 100, 1134
- Carpenter J. M., 2000, *AJ*, 120, 3139
- Carpenter J. M., 2001, *AJ*, 121, 2851
- Chambers K. C., Magnier E. A., Metcalfe N., et al., 2019, preprint (arXiv:1612.05560v4)
- Chavarría L. A., Allen L. E., Hora J. L., et al., 2008, *ApJ*, 682, 445
- Cohen J. G., Frogel J. A., Persson S. E., et al., 1981, *ApJ*, 249, 481
- Crampton D., & Fisher W. A., 1974, *PDAO*, 14, 283
- Danks A. C., Dennefeld M., 1994, *PASP*, 106, 382
- Dewangan L. K., Baug T., Ojha D. K., et al., 2017, *ApJ*, 845, 34
- Drew J. E., Greimel R., Irwin M. J., et al., 2005, *MNRAS*, 362, 753
- Dutta S., Mondal S., Jose J., et al., 2015, *MNRAS*, 454, 3597
- Dutta S., Mondal S., Samal M. R., et al., 2018, *ApJ*, 864, 154
- Elias J. H., Frogel J. A., Matthews K., et al., 1982, *AJ*, 87, 1029
- Elmegreen B. G., Lada C. J., 1977, *ApJ*, 214, 725
- Elmegreen B. G., 1998, in *ASP Conf. Ser. 148, Origins*, ed. C. E. Woodward, J. M. Shull & H. A. Thronson (San Francisco, CA:ASP), 150
- Fazio G. G., Hora J. L., Allen L. E., et al., 2004, *ApJS*, 154, 10
- Flaherty K. M., Pipher J. L., Megeath S. T., et al., 2007, *ApJ*, 663, 1069
- Fukuda N. & Hanawa T., 2000, *ApJ*, 533, 911
- Gaia Collaboration, Brown A. G. A., Vallenari A., et al., 2018, *A&A*, 616, A1
- Gaia Collaboration, Prusti, T., Bruijne J. H. J., et al., 2016, *A&A*, 595, A1
- Girardi L., Bertelli G., Bressan A., et al., 2002, *A&A*, 391, 195
- Gutermuth R. A., Megeath S. T., Myers P. C., et al., 2009, *ApJS*, 184, 18



- Gutermuth R. A., Megeath S. T., Pipher J. L., et al., 2005, *ApJ*, 632, 397
- Gutermuth R. A., Myers P. C., Megeath S. T., et al., 2008, *ApJ*, 674, 336
- Hatchell J., Fuller G. A., Richer J. S., et al., 2007, *A&A*, 468, 1009
- Herbst W., Herbst D. K., Grossman E. J., et al., 1994, *AJ*, 108, 1906
- Herbst W., Shevchenko V. S., 1999, *AJ*, 118, 1043
- Hernández J., Calvet N., Briceño C., et al., 2004, *AJ*, 127, 1682
- Hillenbrand L. A., Bauermeister A., & White R. J., 2008, *ASP Conference Series*, Vol. 384, 14th Cambridge Workshop on Cool Stars, Stellar Systems, and the Sun, 200
- Hora J. L., Marengo M., Park R., et al., 2012, *Proc. SPIE*, 8442, 39
- Hunter D. A., & Massey P., 1990, *AJ*, 99, 846
- Jacoby G. H., Hunter D. A., Christian C. A., 1984, *ApJS*, 56, 257
- Jose J., Pandey A. K., Samal M. R., et al., 2013, *MNRAS*, 432, 3445
- Kobulnicky H. A., Lundquist M. J., Bhattacharjee A., et al., 2012, *AJ*, 143, 71
- Lada C. J., Adams F. C., 1992, *ApJ*, 393, 278
- Lada C. J., Lada E. A., 2003, *ARA&A*, 41, 57
- Lada C. J., Lada E. A., Clemens D. P., et al., 1994, *ApJ*, 429, 694
- Lahulla J. F., 1987, *AJ*, 94, 1062
- Landolt A. U., 1992, *AJ*, 104, 340
- Lundquist M. J., Kobulnicky H. A., Alexander M. J., et al., 2014, *ApJ*, 784, 111
- Luri X., Brown A. G. A., Sarro L. M., et al., 2018, *A&A*, 616, A9
- Magnier E. A., Chambers K. C., Flewelling H. A., et al. 2016a, preprint (arXiv:1612.05240v3)
- Magnier E. A., Schlafly E. F., Finkbeiner D. P., et al. 2016b, preprint (arXiv:1612.05242v3)
- Marigo P., Girardi L., Bressan A., et al. 2017, *ApJ*, 835, 77
- Mayer P., Macák P., 1973, *BAICz*, 24, 50
- Meyer M. R., Calvet N., & Hillenbrand L. A., 1997, *AJ*, 114, 288
- Ojha D. K., Samal M. R., Pandey A. K., et al., 2011, *ApJ*, 738, 156
- Ojha D. K., Tamura M., Nakajima Y., et al., 2004, *ApJ*, 608, 797
- Oke J. B., 1990, *AJ*, 99, 1621
- Palla F. & Stahler S. W., 2002, *ApJ*, 581, 1194
- Pecaut M. J. & Mamajek E. E., 2013, *ApJS*, 208, 9
- Porras A, Christopher M, Allen L., et al., 2003. *AJ*, 126, 1916
- Puget P., Stadler E., Doyon R., et al., 2004, *Proc. SPIE*, 5492, 978
- Sagar R., Kumar B., Omar A., et al., 2012, *Proc. SPIE*, 8444E, 1
- Santos-Silva T. & Gregorio-Hetem J., 2012, *A&A*, 547, A107
- Saral G., Hora J. L., Audard M., et al., 2017, *ApJ*, 839, 108
- Saral G., Hora J. L., Willis S. E., et al., 2015, *ApJ*, 813, 25
- Schlafly E. F., Finkbeiner D. P., Jurić M., et al., 2012, *ApJ*, 756, 158
- Schlafly E. F., Meisner A. M., Stutz A. M., et al., 2016, *ApJ*, 821, 78
- Skrutskie M. F., Cutri R. M., Stiening R., et al., 2006, *AJ*, 131, 1163
- Stetson P. B., 1987, *PASP*, 99, 191
- Stetson P. B., 1992, in *Astronomical Society of the Pacific Conference Series*, Vol. 25, *Astronomical Data Analysis*
- Stubbs C. W., Doherty P., Cramer C., et al., 2010, *ApJS*, 191, 376
- Sung H., Chun M. Y., Bessel M. S., 2000, *AJ*, 120, 333
- Tody D., 1986, *Proc. SPIE*, 627, 733
- Tody D., 1993, in *ASP Conf. Ser. 52, Astronomical Data Analysis Software and Systems II*, ed. R. J. Hanisch, R. J. V. Brissenden, & J. Barnes (San Francisco, CA: ASP), 173
- Tonry J. L., Stubbs C. W., Lykke K. R., et al., 2012, *ApJ*, 750, 99
- Torres-Dodgen A. V., Weaver W. B., 1993, *PASP*, 105, 693
- Walborn N. R., Fitzpatrick E. L., 1990, *PASP*, 102, 379
- Wang W.-H., Cowie L. L., Barger A. J., et al., 2010, *ApJS*, 187, 251
- York D. G., Adelman J., Anderson J. E., et al., 2000, *AJ*, 120, 1579